Supporting information for

Spin coherence and relaxation dynamics of localized electrons and holes in $FAPbI_3$ films

G. Lagüe [1], F. Bernardot [1], V. Guilloux[1], L Legrand [1], T. Barisien [1], J. Sánchez-Diaz [2], S. Galve-Lahoz [2], I. Saïdi [3], K. Boujdaria [3], J. P. Martinez-Pastor [4], C. Testelin [1], I. Mora-Seró [2] and M. Chamarro [1]

[1]*Sorbonne Université, CNRS, Institut des NanoSciences de Paris, Paris, France.*
[2] *Institute of Advanced Materials (INAM), Universitat Jaume I, Castelló de la Plana, Spain.*
[3] *Université de Carthage, Faculté des Sciences de Bizerte, LR01ES15 Laboratoire de Physique des Matériaux : Structure et Propriétés,7021 Zarzouna, Bizerte, Tunisia.*
[4] *UMDO, Instituto de Ciencia de los Materiales, Universidad de Valencia, Valencia, Spain.*

e-mail: chamarro@insp.jussieu.fr

15 pages, 5 Figures and 4 Tables.

Table of contents

S1: Sample preparation

Materials

Formamidinium iodide (FAI, 98%) was obtained from Greatcell solar. Lead iodide (PbI_2, 98%) was obtained from TCI. N, N-dimethylformamide (DMF, anhydrous, 99.9%), N-methyl-2-pyrrolidone (NMP, anhydrous, 99.9%) and diethyl ether (anhydrous, >99.8%) were obtained from Sigma Aldrich. All the materials are reagent grade and were used without further purification.

$FAPbI_3$ film preparation

The perovskite film was deposited on borosilicate substrates which were cleaned by an ultrasonic bath with ethanol, acetone, and isopropanol for 15 minutes each; then the substrates were dried with an N_2 flow. Before the $FAPbI_3$ deposition, the substrates were treated for 10 minutes in a UV-ozone chamber. The $FAPbI_3$ perovskite solution was prepared by dissolving 461 mg of PbI_2 (1 mmol) and 172 mg of FAI (1 mmol) in 96.30 µL of NMP (1 mmol) and 590.71 µL of DMF; the solution was heated at 60 °C for 2 hours until all the precursors were completely dissolved. 70 µL of perovskite solution was spin-coated on top of the borosilicate substrates at 5500 rpm for 17 seconds and 450 µL of diethyl ether was dropped on the spinning substrate 9 seconds after starting the spinning process. After the spinning process, the substrates were annealed at 100 °C and 165 °C for 1 minute and 10 minutes, respectively. The film deposition was performed in ambient air conditions (50-60 %RH)[1].

S2: Absorption and photoluminescence measurements

Steady-state visible absorption

Absorption spectra as a function of temperature have been acquired with a Cary 5000 spectrometer. Low temperature (down to » 10 K) measurements were done resorting to an exchange gas cryostat inserted in the spectrometer main chamber.

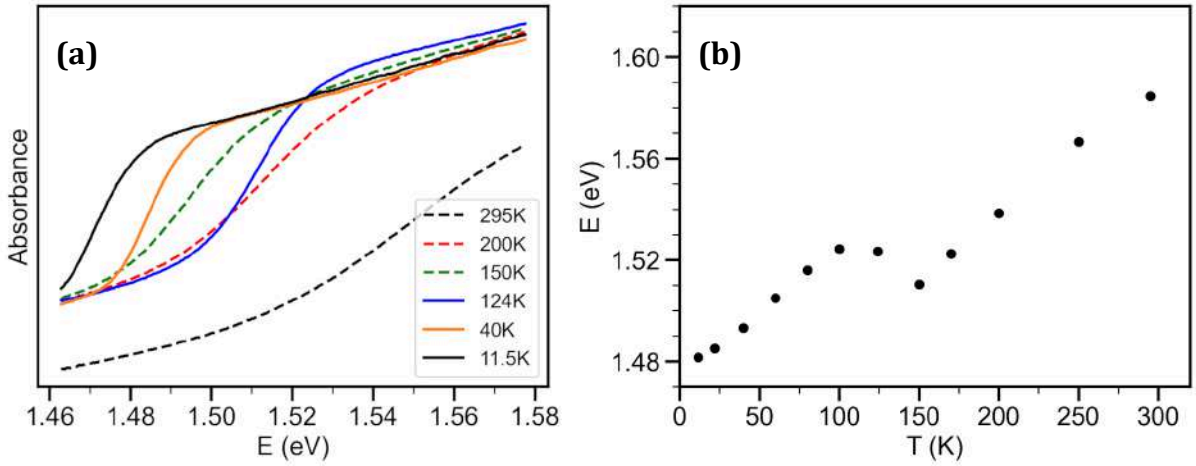

Figure S1: **(a)** Absorption spectra of $FAPbI_3$ at different temperatures. **(b)** Near band-edge maximum energy in the absorption spectra as a function of the temperature; we can observe the phase transition the $FAPbI_3$ sample undergoes between 100 and 150 K.

When cooling down the sample, we observe an increase in the energy of the absorbed light below 150 K. Previous works have shown that $FAPbI_3$ undergoes a phase transition at this temperature[2].

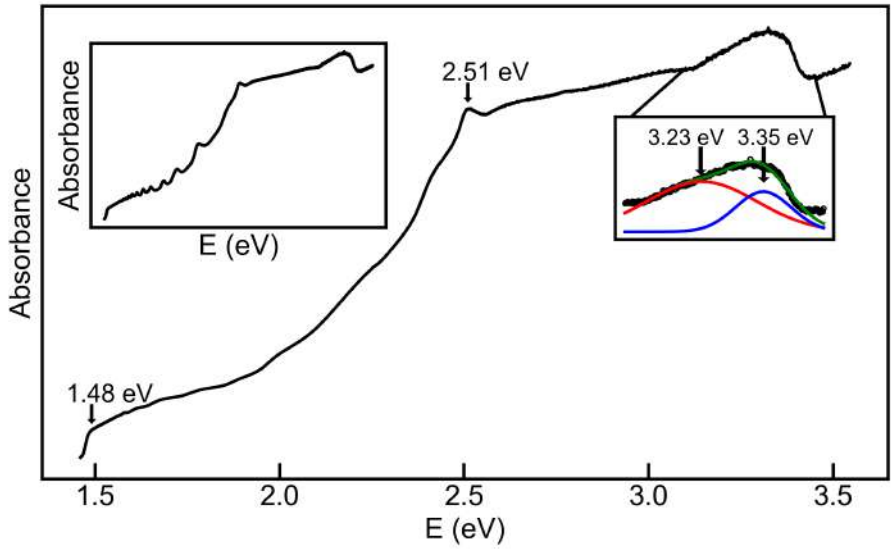

Figure S2: Absorption spectrum of $FAPbI_3$ at 10K after analyse proposed in ref. 3 Inset left: Raw low-temperature absorption spectrum without the post-processing proposed in ref 3. Inset right: zoom on the region 3,08 eV to 3.47 eV and the fit to two broad peaks (red and blue lines).

The absorption spectrum of $FAPbI_3$ measured at 10K shows oscillations already observed and explained by other authors[3,4]. We applied the procedure proposed by

these authors to obtain the absorption spectrum of $FAPbI_3$ films without oscillations. We also verified that the peaks observed in the blue side of the absorption spectrum are not related to the absorption of the glass substrate, which shows a very flat response in this region. In the spectrum obtained after analysis, we observe the absorption edge due to exciton absorption and, mainly, two peaks. One at 2.51 eV and another broader one, in the energy region between 3.08 and 3.47 eV which is the result of two bands (see zoom in figure S2).

CW-photoluminescence

The PL excitation is fixed to 820 nm (Ti:Sapphire laser, pulse width of ≈ 2 ps, 80 MHz repetition rate). The signal is analyzed thanks to a 75-cm-focal-length spectrometer (Acton sp2750i, Princeton Instruments) which is coupled to a nitrogen-cooled CCD (SPEC10, Princeton Instruments).

Time-resolved luminescence

For time-resolved photoluminescence measurements, the excitation is set to 410 nm.
We use a streak-camera synchronized with the high repetition rate Ti:Sapphire laser (15 ps resolution, C5680 model from Hamamatsu incorporating a M5675 synchroscan unit) and coupled to the Acton spectrometer.
Experiments are performed with a homemade confocal-like setup using a large working-distance microscope objective (NA ≈ 0.6) to focus light on film and collect its emission in a reflection configuration. The film is glued on the coldfinger of a cryostat designed for thermal expansion compensation (from Oxford Instrument Company).

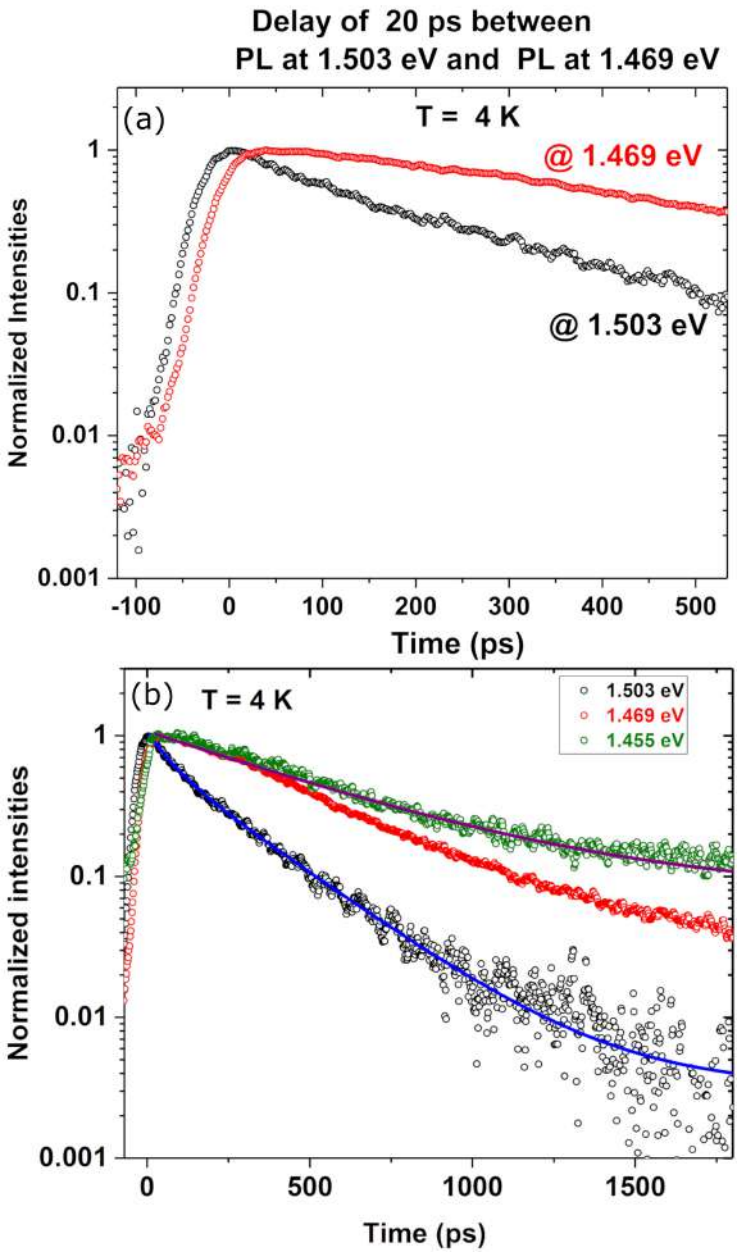

Figure S3: **(a)** Time resolved luminescence decays for two detection energies. For detection at energy 1.469 eV, we observe a small rise time**. (b)** Time-resolved luminescence decays obtained at 4 K and detected at different energies: 1.503, 1.469 and 1.455 eV.

The time-resolved PL spectrum at 4 K detected at 1.503 eV shows a double exponential decay with two time constants: 70 ps and 265 ps. We underline that the latter time is slightly slower than the shortest time obtained by PFR measurements in Faraday geometry (100-200 ps), and therefore these two times are associated to the same state.
When detection moves towards lower energies, we observe a short rise time and an exponential decay with a characteristic time that becomes longer. At 1.455 eV, the adjustment is a single exponential law with a time constant of 530 ps and with a residual value (a plateau) close to 5 % of the maximum.

S3: Photo-induced Faraday rotation (PFR) measurements

We used a degenerate pump-probe technique, the PFR, which is well-adapted to study spin relaxation and decoherence times of both excited states and resident electrons or holes. Laser pulses with a 2 ps duration were generated by a Ti:Sapphire mode-locked oscillator at 75.8 MHz. The pump beam polarization is σ^+/σ^- modulated at 100 kHz with an electro-optic modulator (average intensity ≈ 1 W/mm^2); the probe beam is linearly polarized. After transmission through the sample, the probe beam is analyzed into its vertical and horizontal components, and the difference in their intensity is measured in a balanced optical bridge. To improve the signal-to-noise ratio, a single lock-in amplifier is used. The sample was placed in a liquid-helium cryostat containing a superconducting coil and cooled down to 2 K.

PFR experiments in Voigt geometry were performed at lower energy (E = 1.47 eV). The results were very close to the ones obtained at 1.48 eV and no significant difference in the spin properties were observed.

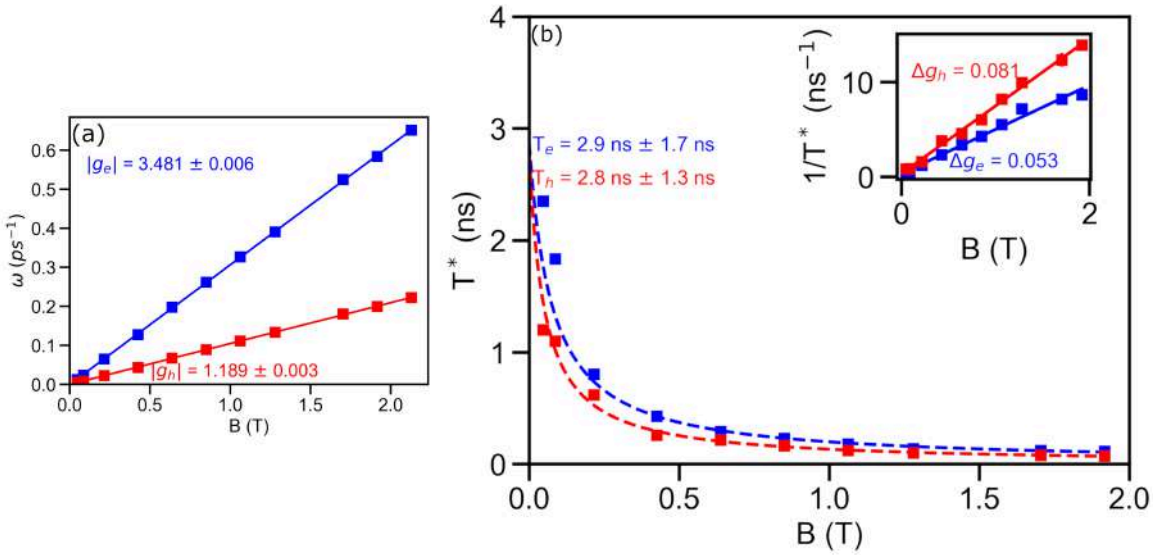

Figure S4: Electron and hole Landé factors and spin dephasing time with pump and probe beams at 1.47eV.

S4: Experimental results in halide perovskites: Landé factors, dephasing and relaxation times

Pb-based HP crystals	E_g (eV)	T_1 (ns)	$T(0)_{2e}$ (ns)	$T(0)_{2h}$ (ns)	g_e^{min}	g_e^{max}	g_h^{min}	g_h^{max}
$FA_{0.9}Cs_{0.1}PbI_{2.8}Br_{0.2}$ [5, 6]	1.527	45	8	5.5	3.48	3.72	-1.29	-1.15
$MAPbI_3$ [6, 7]	1.652	≤ 37	0.4	2.7	2.46	2.98	-0.71	-0.28
$MAPbI_3$ [8]	1.63		11	6	2.52	2.63	-0.57	-0.28
$FAPbBr_3$ [6]	2.189				2.32	2.44	0.36	0.41
$MAPbBr_3$ [9]	2.25		1.5 (@50mT)	8 (@100mT)	1.75	2.15	0.42	0.6
$CsPbBr_3$ [6]	2.352				1.69	2.06	0.65	0.85
$CsPbBr_3$ [10]	2.352	53-32	≤ 5.2	1		1.92		0.75
$CsPbBr_3$ [11]	2.33		5.6 (@10mT)	2 (@100mT)	1.82	1.95	0.69	0.76
$MAPbBr_{1.5}Cl_{1.5}$ [6]	2.59				1.47			

Table S1: Experimental values of spin relaxation and dephasing times and Landé factors in Pb-based halide perovskites crystals.

Pb-based HP films	E_g (eV)	T_1 (ns)	$T(0)_{2e}$ (ns)	$T(0)_{2h}$ (ns)	g_e	g_h
$FAPbI_3$ [12]	1.496	17	3.3	2.4	3.447	-1.134
$MAFAPbI_3$ [13]	1.56		0.671	0.721	3.75	-1.24
$MAPbI_3$ [14, 15]	1.635 1.612		4.4 7	3.4 3.7	2.593 2.6-1.6 2.723	-0.238 -0.3, -0.4 -0.350
$MAPbBr_3$ [9]	2.59				1.83	0.55
$CsPbBr_3$ [16]			0.050	0 .282	1.71	0.74
$CsPbBr_3$ [17]	2.33		0.25	0.4	1.78	0.77

Table S2: Experimental values of spin relaxation and dephasing times and Landé factors in Pb-based halide perovskites polycrystalline films.

S5: Tetragonal k.p model in D_{4h} point group

I. Band parameters

To calculate the band diagram of the tetragonal $FAPbI_3$ perovskite with D_{4h} as point group, we use the multiband **k.p** description[18]. We consider 8 valence-band and 6 conduction-band states (spin included). A schematic illustration of the quantum states involved in the present model is shown in Figure S4. The band-gap energy E_g, the energy levels of the second and third conduction bands (E_2 , E_3), and the energy levels of the p-

like valence bands A_i $(i = 1,2,3)$ are represented in Figure S4. The origin of energies is taken at the top of the s-like valence band.

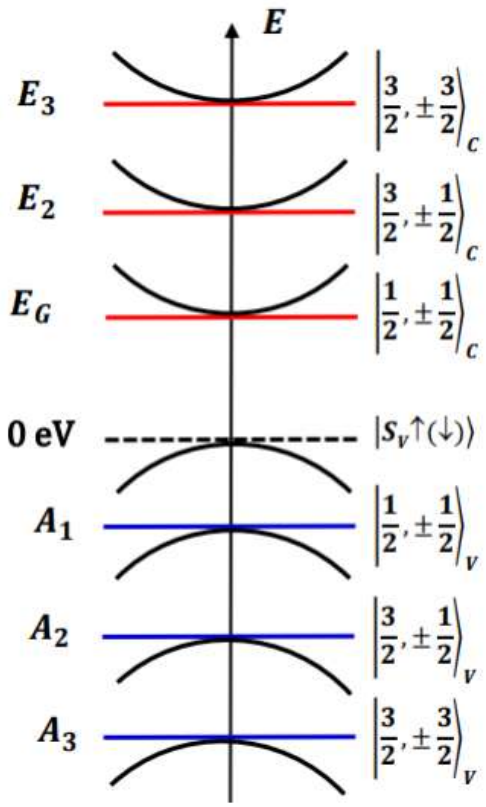

Figure S5: Schematic representation of the dispersion relations of a perovskite semiconductor such as $FAPbI_3$. We designate the first four doubly degenerate valence band states as $|S_V \uparrow (\downarrow)\rangle$, $\left|\frac{1}{2},\pm\frac{1}{2}\right\rangle_V$, $\left|\frac{3}{2},\pm\frac{1}{2}\right\rangle_V$ and $\left|\frac{3}{2},\pm\frac{3}{2}\right\rangle_V$. The first three doubly degenerate conduction band states are $\left|\frac{1}{2},\pm\frac{1}{2}\right\rangle_C$, $\left|\frac{3}{2},\pm\frac{1}{2}\right\rangle_C$ and $\left|\frac{3}{2},\pm\frac{3}{2}\right\rangle_C$. Horizontal lines are illustrating the band-gap energy, E_g, energy levels of the second and third conduction band states (E_2, E_3), and energy levels of p-like valence bands A_i, $(i = 1,2,3)$. The energy origin is assumed to be at the top of the upper valence band.

Table S3 provides the **k.p** parameters for $FAPbI_3$, as well as for $CsPbBr_3$ and $MAPbI_3$.

k.p parameters	$FAPbI_3$ (this work)	$MAPbI_3$	$CsPbBr_3$
E_g (eV)	1.52	1.65	2.36
E_2 (eV)	2.844	3.47	3.68
E_3 (eV)	2.978	3.67	3.83
A_1 (eV)	-1.21	-1.62	-1.82
A_2 (eV)	-1.46	-1.88	-1.84
A_3 (eV)	-1.58	-1.98	-1.84
Δ_{SO} (eV)	1.375	1.42	1.32
T (eV)	0.208	0.319	240
θ (degrees)	39.54	40.02	40.19
$E_{P_{S,\rho}}$ (eV)	14.60	11.29	11.6
$E_{P_{S,z}}$ (eV)	14.85	11.96	14.04
$E_{P_{X,1}}$ (eV)	9.93	10.59	3.11
$E_{P_{X,2}}$(eV)	9.98	2.75	4.78
$E_{P_{X,3}}$ (eV)	6.89	6.29	2.04

TABLE S3: Summary of $FAPbI_3$ bulk band parameters values that were generated using the **k.p** theory. E_g denotes the bulk band-gap energy, E_2 and E_3 indicate the energy levels of the second and third conduction bands, Δ_{SO} denotes the spin-orbit coupling, A_i $(i = 1,2,3)$ indicate the energy levels of p-like valence bands, T denotes the tetragonal crystal field, θ is the phase angle defined as $\tan 2\theta = 2\sqrt{2}\Delta_{SO}/(\Delta_{SO} - 3T)$ (with $0 < \theta < \pi/2$). $E_{P_{S,\rho}}, E_{P_{S,z}}$ are the Kane energies in tetragonal phase and defined as $E_{P_{S,\ell}} = (\frac{2m_0}{\hbar^2})\left|P_{S,\ell}\right|^2$. $E_{P_{X,i}}$ are the coupling energies between the p-like valence states and the p-like conduction states. The band parameters of $CsPbBr_3$ and $MAPb_3$, which were determined in our previous studies[19, 20, 21] using the multiband **k.p** theory, are also provided in the Table.

The tetragonal crystal field, T, the spin-orbit coupling, Δ_{SO} are related with energies E_G, E_2 and E_3 by the following expressions:

$$\left(E_3 - E_g\right) = \frac{1}{2}(T + \Delta_{SO}) + \frac{1}{2}\left(E_2 - E_g\right) \quad (1)$$

$$\left(E_2 - E_g\right) = \sqrt{\Delta_{SO}^2 + T^2 - \frac{2}{3}T\Delta_{SO}} \quad (2)$$

That is why we can estimated from spectroscopic experimental measurements the values of T and Δ_{SO} and by using $\tan 2\theta = 2\sqrt{2}\Delta_{SO}/(\Delta_{SO} - 3T)$ the value of θ.

From low-temperature absorption spectrum (see FigureS2), we can experimentally obtain E_g, E_2 and E_3. $E_g \approx 1.49$ eV is obtained by adding the binding energy (14meV) to the edge energy 1.48eV. Taking into account DFT calculations for the tetragonal phase crystal (space group $P4/mbm$)[22] of $FAPbI_3$, we conclude that the observed peak at 2.51

eV corresponds to transitions at k-points different from the Z point (k-point for the direct gap) and that the broad bands at 3.23 and 3.35 eV are associated with optical transitions at E_2 and E_3 energies respectively. In the case of $FAPbI_3$, when we introduce in expressions (1) and (2) the optical transition energies determined by the low-temperature absorption spectrum (Figure S2), we obtain T= 0.187 eV, Δ_{SO} = 1.79 eV and $\theta = 38{,}17°$. These values even if they are different from the calculated values given in Table S3, compare well with theoretical values.

II. Numerical results for Landé g-factors

The Landé g-factor results from the Cartesian components of **k** = (k_x, k_y, k_z) which no longer commute due to the presence of a weak static magnetic field **B** = (B_x, B_y, B_z). The commutator of two components of **k** is:

$$\left[k_\alpha, k_\beta\right] = -i\frac{e}{\hbar}\,\epsilon_{\alpha\beta\gamma}B_\gamma \qquad (3)$$

where $\alpha, \beta, \gamma = x, y, z$ denote the Cartesian components and $\epsilon_{\alpha\beta\gamma}$ is the Levi-Civita symbol.

The carriers Landé g-factors for Pb-based halide perovskites with tetragonal symmetry (D_{4h} as point group) are anisotropic and can be represented by a second rank tensor.

The Zeeman Hamiltonian for the upper s-like valence band[23] is given by:

$$\mathcal{H}_Z^h = \frac{\mu_B}{2}\left[g_{h\parallel}\sigma_z B_z + g_{h\perp}\left(\sigma_x B_x + \sigma_y B_y\right)\right] \qquad (4)$$

where μ_B is the Bohr magneton, $g_{h\parallel}$ ($g_{h\perp}$) denotes the component of the hole g-factor tensor parallel (perpendicular) to the tetragonal **c**-axis and $\sigma = (\sigma_x, \sigma_y, \sigma_z)$ is the vector formed by the Pauli matrices. The straightforward application of the method detailed in Ref[18] leads to:

$$\begin{cases} g_{h\parallel} = g_0 + E_{P_{S,\rho}}\left[\frac{1}{E_3} - \frac{sin^2\theta}{E_2} - \frac{cos^2\theta}{E_g}\right] \\ g_{h\perp} = g_0 + sin\theta\, cos\theta\sqrt{2E_{P_{S,\rho}}E_{P_{S,z}}}\left[\frac{1}{E_2} - \frac{1}{E_g}\right] \end{cases} \qquad (5)$$

where $g_0 = 2.0023$ is the free electron Landé factor, ($E_{P_{S,\rho}}, E_{P_{S,z}}$) are the Kane energies in the tetragonal symmetry, and θ is the Bloch function parameter.

Moreover, we can write the Zeeman Hamiltonian for the lowest p-like conduction bands[21, 23]as:

$$\mathcal{H}_Z^e = -\mu_B(1+3\kappa_1)L_z B_z - \mu_B(1+3\kappa_2)\left(L_x B_x + L_y B_y\right) + \mu_B \boldsymbol{\sigma_e}.\boldsymbol{B} \qquad (6)$$

where (κ_1, κ_2) are the Luttinger magnetic parameters[24] and $\boldsymbol{L} = (L_x, L_x, L_x)$ ($\ell = 1$) is the angular momentum.

The electron g-factor tensor components are derived with the same method as mentioned in Ref[21]. We obtain:

$$g_{e\parallel}^{T-14b} = -2(cos^2\theta - sin^2\theta) + \frac{E_{P_{S,\rho}} cos^2\theta}{E_g} - \frac{E_{P_{X,3}} sin^2\theta}{(E_g - A_3)} + \frac{E_{P_{X,3}} sin^4\theta - E_{P_{X,2}} cos^4\theta}{(E_g - A_2)}$$
$$+ sin^2\theta\, cos^2\theta\, \frac{E_{P_{X,3}} - E_{P_{X,2}}}{(E_g - A_1)} - 2(1 + 3\bar{\kappa}_1) cos^2\theta \quad (7)$$

$$g_{e\perp}^{T-14b} = -2\, sin^2\theta\ - sin\theta\, cos\theta \sqrt{2E_{P_{X,1}} E_{P_{X,3}}} \left[\frac{sin^2\theta}{(E_g - A_2)} + \frac{cos^2\theta}{(E_g - A_1)}\right]$$
$$+ sin\theta\, cos\theta \frac{\sqrt{2E_{P_{S,\rho}} E_{P_{S,z}}}}{E_g} - 2\sqrt{2}(1 + 3\bar{\kappa}_2) sin\theta\, cos\theta \quad (8)$$

where $E_{P_{X,i}}$ (i=1, 2, 3) are the energies associated to the corresponding interband momentum matrix elements. The contributions from the remote bands have been considered via the Luttinger parameters $\bar{\kappa}_{1,2}$.

The Equations (5) for holes and (7-8) for electrons are used to calculate the carriers Landé factors. Table S4 summarizes our theoretical results obtained for $FAPbI_3$, $CsPbBr_3$ and $MAPbI_3$ in the absence of the Luttinger corrections ($\bar{\kappa}_1 = \bar{\kappa}_2 = -1/3$). We also include in Table S4, the numerical results of the exciton g-factor tensor, $g_{X\parallel} = g_{e\parallel} + g_{h\parallel}$ and $g_{X\perp} = g_{e\perp} + g_{h\perp}$.

Pb-based HP **k.p** theory tetragonal model	E_g (eV)	$g_e^{\parallel}$	$g_e^{\perp}$	$g_h^{\parallel}$	$g_h^{\perp}$	$g_{X\parallel}$	$g_{X\perp}$
$FAPbI_3$	1.52	3.355	3.883	-0.888	-1.128	2.467	2.755
$MAPbI_3$	1.65	3.250	2.329	-0.280	-0.570	2.97	1.759
$CsPbBr_3$	2.36	1.867	2.515	0.852	0.653	2.719	3.168

TABLE S4: Carriers Landé g-factors calculated from Eq. (3) for holes and Eqs. (5-6) for electrons. The exciton g-factors are also provided.

REFERENCES

[1]Muhammd Salim, K.M.; Masi, S.; Gualdon-Reyes, A.F.; Sanchez, R.S.; Barea, E.M.; Krêsmarovà, M; Sanchez-Roy J.F. and Mora-Serò, I., Boosting long-term Stability of pure Formamidinium perovskte solar cells by ambient air additive assisted fabrication. *ACS Energy Lett.* 2021, 6, 10, 3511-3521.

[2] Stoumpos C. C., Malliakas C. D., and Kanatzidis M. G. *Inorganic Chemistry* **2013** *52* (15), 9019-9038

[3] Wright A.D.; Volonakis G. ; Borchert J.; Davies C.L.; Giustino F.; Johnston M.B. and Herz L.M. Intrinsic quantum confinement in formamidinium lead triiodide perovskite. *Nat. Mater*. **2020**,19(11), 1201-1206.

[4]Elmestekawy K.A. ; Wright A.D; Lohmann K.B.; Borchert J.; Johnston M.B. and Herz L.M .Controlling intrinsic quantum confinement in formamidinium lead triiodide perovskite throught Cs substitution. *ACS Nano* **2022**, 16, 9640-9650.

[5] Kirstein, E. Coherent spin dynamics and carrier-nuclear interaction in lead halide perovskite crystals, TU Dortmund, Dortmund, Germany, 2022. http://dx.doi.org/10.17877/DE290R-22888

[6] Kirstein, E, Yakovlev DR ; Glazov, MM ; Zhukov, EA, Kudlacik D, Kalitukha, I.V. ; Sapega, V.F. ; Dimitriev, G.S., Semina, M. A.; Nestoklon, M. O.; Ivchenko, E. L.; Kopteva, N. E.; Dirin, D. N.; Nazarenko, Kovalenko, M.V.;Baumann,A.;Höcker,J.;Dyakonov, V.; Bayer, M. The Lande factors of electrons and holes in lead halide perovskites: universal dependence on the band gap. Nat. Commun. 2022, 13, 3062.

[7] Kirstein, E.; Yakovlev, D. R.; Zhukov, E. A.; Höcker, J.; Dyakonov, V.; Bayer, M. Spin dynamics of electrons and holes interacting with nuclei in MAPbI3 perovskite single crystals. ACS Photonics 2022, 9, 1375–1384.

[8] Huynh, U. N.; Liu, Y.; Chanana, A.; Khanal, D. R.; Ser- cel, P. C.; Huang, J.; Vardeny, Z. V. Transient quantum beatings of trions in hybrid organic triiodine perovskite single crystal. Nat. Commun. 2022, 13, 1428.

[9] Huynh U.N. ; Bodin R. ; Pan X. ; Bailey P. ; Liu H. ; McGill S. ; Semenov D. ; Sercel P. C. ; and Valy Vardeny Z. Magneto-optical studies of hybrid organic/inorganic perovskite: The case of methyl-ammonium lead bromide. Phys. Rev. B, 2024, 109, 014316.

[10] Belykh, V. V.; Yakovlev, D. R.; Glazov, M. M.; Grigoryev, P. S.; Hussain, M.; Rautert, J.; Dirin, D. N.; Kovalenko, M. V.; Bayer, M. Coherent spin dynamics of electrons and holes in CsPbBr3 perovskite crystals. Nat. Commun. 2019, 10, 673.

[11] Huynh U. N. ; Feng T. ; Khanal D. R. ; Liu H. ; Bailey P., Bodin R., Sercel P. C., Huang J. ; and Vardeny Z. V. Transient and steady state magneto-optical studies of the $CsPbBr_3$ crystal Phys. Rev B 2022, 106, 094306.

[12] This work

[13] Zhang H., Zhai Z., BI Z., Gao H., Ye M., Xu Y., Tan H. and Yang L. Spin Coherence and spin relaxation in hybrid organic-inorganic lead and mixed lead-tin perovskites. *Nano Lett*. 2023, 23, 7914-7920.

[14] Garcia-Arellano, G.; Trippe-Allard, G.; Legrand, L.; Barisien, T.; Garrot, D.; Deleporte, E.; Bernardot, F.; Testelin, C.; Chamarro, M. Energy tuning of electronic spin coherent evolution in methylammonium lead iodide perovskites. *J. Phys. Chem. Lett.* 2021 12, 8272–8279.

[15] Garcia-Arellano, G.; Trippe-Allard, G.; Campos, T.; Bernardot, F.; Legrand, L.; Garrot, D.; Deleporte, E.; Testelin, C.; Chamarro, M. Unexpected anisotropy of the electron and hole Lande g-factors in perovskite CH3NH3PbI3 polycrystalline films. Nanomaterials 2022, 12, 1399.

[16] Jacoby L.M ; Crane M.J. and Gamelin D.R. Coherent Spin Dynamics in Vapor-Deposited $CsPbBr_3$ Perovskite Thin Films. *Chem. Mater.* 2022, 34, 4, 1937–1945

[17] Grigoryev P.S. ; Belikh V.V. ;Yakovlev D.R. ; Lhuillier E and Bayer M Coherent spin dynamics of electrons and holes in CsPbBr3 colloidal nanocrystals Nano Lett. 2021, 21, 8481-8487.

[18] Ben Aich, R. ; Ben Radhia, S. ; Boujdaria, K. ; Chamarro M. ; and Testelin C. Multiband k·p Model for Tetragonal Crystals: Application to Hybrid Halide Perovskite Nanocrystals *The Journal of Physical Chemistry Letters* **2020** *11* (3), 808-817.

[19] Ghribi, A.; Ben Aich, R.; Boujdaria, K.; Barisien, T.; Legrand, L.; Chamarro, M.; Testelin, C. Dielectric Confinement and Exciton Fine Structure in Lead Halide Perovskite Nanoplatelets. *Nanomaterials* **2021**, *11*, 3054. https://doi.org/10.3390/nano11113054

[20] Ghribi, A.; Ben Radhia, S.; Boujdaria, K.; Legrand, L.; Barisien, T.; Chamarro, M. and Testelin, C. Dielectric effects, crystal field, and shape anisotropy tuning of the exciton fine structure of halide perovskite nanocrystals *Phys. Rev. Materials*. 2022, 6, 106001.

[21] Garcia-Arellano, G.; Boujdaria, K.; Chamarro, M.; Testelin, C. Landé g factors in tetragonal halide perovskite: A multiband k.p model *Phys. Rev. B*, 2022, 106, 165201.

[22] Muhammad Z.; Liu P.; Ahmad R.; Jalali-Asadabadi S.; Francini C. and Ahmad I. Revealing the quasi particule electronic and excitonic nature in cubic, tetragonal and hexagonal phases of $FAPbI_3$. AIP Advances **2022**, 12, 025330.

[23] Yu, Z. Effective-mass model and magneto-optical properties in hybrid perovskites. *Sci Rep* **6**, 28576 (2016). https://doi.org/10.1038/srep28576

[24] Luttinger, J. M. Quantum Theory of Cyclotron Resonance in Semiconductors: General Theory *Phys. Rev.* 1956, 102, 1030